Magnetically recoverable MoS2/Fe2O3/graphene oxide ternary Z-scheme heterostructure photocatalyst for wastewater contaminant removal: Mechanism and performance

Journal of Environmental Chemical Engineering 13 (2025) 116813

Contents lists available at ScienceDirect

Journal of Environmental Chemical Engineering

journal homepage: www.elsevier.com/locate/jece

Magnetically recoverable MoS_2/Fe_2O_3/graphene oxide ternary Z-scheme heterostructure photocatalyst for wastewater contaminant removal: Mechanism and performance

L. Vishoda Samarasinghe [a,*], Shobha Muthukumaran [b], Kanagaratnam Baskaran [a]

[a] Faculty of Science, Engineering and Built Environment, Deakin University, VIC 3216, Australia
[b] Institute for Sustainability Industries and Liveable Cities, College of Sport, Health & Engineering, Victoria University, Melbourne, VIC 8001, Australia

ARTICLE INFO

Keywords:
Photocatalytic degradation
Visible-light
Methylene blue
Molybdenum disulfide
Iron (III) oxide
Graphene oxide

ABSTRACT

Water pollution caused by organic contaminants poses a severe threat to human health and ecosystems due to their high toxicity and stability. Herein, MoS_2/Fe_2O_3/GO (MFG) heterojunction composites were synthesized through ball milling and ultrasonication and used for the degradation of dye from wastewater. The as-synthesized optimal MFG composite with an optimal ratio of 2:1:1 exhibited remarkable photocatalytic activity towards Methylene Blue degradation, achieving a 97.90 % degradation in 3 hours under solar simulated irradiation and 88.2 % degradation under natural sunlight, compared to its individual components. Characterization of the composite photocatalyst revealed unique Fe_2O_3 decoration on the MoS_2 and GO matrix, forming an intimate interface heterojunction. This structural arrangement facilitated efficient charge carrier separation, extended the visible light absorption and subsequently improved the photocatalyst's dye degradation and redox capabilities. The experimental data showed that the photodegradation process followed pseudo-first-order kinetics at 22C. Quenching experiments were conducted to elucidate in detail the probable photocatalytic mechanism, which was identified as the Z-scheme mechanism. The reusability experiments showed that the photocatalyst exhibited excellent stability and reusability, maintaining a degradation efficiency of 94.32 % after four successive cycles. Overall, this research demonstrates a facile pathway to synthesize a highly efficient, stable, and easily recoverable, magnetic photocatalyst, addressing the critical issue of textile wastewater pollution.

1. Introduction

The swift advancement of industrialization and urban growth, along with an expanding global population has resulted in a significant rise in contamination of water sources on a worldwide scale. According to data provided by the World Bank, about 17–20 % of water pollution is due to activities within the textile and dyeing industries [1]. Currently, over 100,000 commercial dyes exist in the market with approximately 10,000 being consumed every year. Methylene blue (MB) is a type of thiazine dye with a cationic surface commonly found in textile wastewater and is known for its neurotoxic effects on the central nervous system [2]. This chemical compound has been scientifically observed to possess teratogenic and embryotoxic properties, as evidenced by a Lethal dose50 value of 1180 mg/kg [3]. Additionally, MB exhibits carcinogenic properties and is resistant to biodegradation because of the inherent stability of its aromatic ring within its molecular structure.

During the past few decades, a plethora of advanced technologies have been developed to address this pertinent concern. Some of these include adsorption, coagulation/flocculation, membrane filtration, electrochemical oxidation, precipitation and ozonation [4–6]. However, these techniques suffer from several disadvantages such as the production of secondary waste such as sludge and harmful gases that require additional treatment, high cost of regeneration, prolonged treatment times, and poor efficiency at low concentrations [7,8]. For instance, various adsorbents, including synthetic and natural-derived materials, such as porous carbon, silica, clay, metal-organic frameworks (MOFs) and covalent-organic frameworks (COFs) have been widely employed to remove dye from contaminated wastewater [9]. Zhang et al. synthesized a highly efficient nitrogen self-doped biochar adsorbent for the removal of Rhodamine B and Congo red [10]. This adsorbent removed 100 % of

* Correspondence to: 75 Pigdons Rd, Waurn Ponds, VIC 3216, Australia.
E-mail address: vishodasamarasinghe@gmail.com (L.V. Samarasinghe).

https://doi.org/10.1016/j.jece.2025.116813
Received 25 October 2024; Received in revised form 21 March 2025; Accepted 26 April 2025
Available online 1 May 2025

the dye when the dosage was increased to 12.5 mg but needed to be regenerated using a mixture of acetic acid and hydrogen peroxide which led to secondary pollution. Naushad et al. synthesized arginine-modified activated carbon for the removal of MB from aqueous media [11]. The adsorbent removed 88 % of the initial MB concentration but dropped to 75 % upon the 4th recycling experiment and used HCl solution for regeneration. In another study metal ion chelation flocculation followed by flotation separation was proposed for congo red removal from simulated wastewaters [12]. Over 99 % of the dye was removed although regeneration after adsorption was complicated. Alternatively, photocatalytic treatment technology provides several benefits compared to the conventional dye removal techniques such as high efficacy, environment friendliness and, cost-effectiveness. Moreover, this treatment technology causes complete degradation, causing no secondary pollution, and is highly effective even at low concentrations [8]. A primary limitation hindering the practical use of photocatalysis has been the high recombination rate of the photogenerated charge carriers which lowers the efficiency of the process [13,14]. To mitigate this, researchers have been exploring various blends of multi-functional materials to be used as photocatalysts with improved efficiency.

Recently, Molybdenum disulfide (MoS_2) has been regarded as a promising catalyst due to its low cost, narrow bandgap, superior chemical and mechanical stability, low toxicity, abundance across the globe, and high electron mobility [15,16]. However, to improve its catalytic properties, bulk MoS_2 needs to be converted to nano MoS_2 which offers a higher surface area-to-volume ratio, more defects which serve as active sites for catalysis and improved charge separation compared to its bulk counterpart [17,18]. Liquid phase exfoliation of bulk MoS_2 is the most reported technique in literature for producing nano MoS_2. However, this method is time-consuming, tedious, requires organic solvents with high surface tensions, results in a very low yield, and cannot be easily scaled up [19]. To overcome these limitations, mechanochemical exfoliation of bulk MoS_2 via ball milling offers a promising approach. The high-energy ball milling process effectively converts mechanical energy to the solid surface, initiating surface chemical reactions through intense compression, shear, and impact forces [20,21]. Moreover, the S-vacancies and the atomic scale holes of MoS_2 can be increased which will in turn improve the catalytic efficiency of MoS_2 and bring down the surface tension close to water. This will enable the use of water in the next step to further exfoliate the MoS_2 without the use of any chemicals or surfactants [22].

Despite the above-mentioned advantages, MoS_2 still suffers from high recombination of photogenerated charge carriers when used alone. Thus, it is mostly used in conjunction with other materials to construct heterojunctions that will improve the overall activity of the composite photocatalyst. For instance, $MoS_2/ZnIn_2S_4$ type I heterojunction photocatalyst was synthesized via hydrothermal method which was able to degrade 98.7 % of Rhodamine B dye [23]. Nikitha et al. developed a chitosan-supported g-C_3N_4-MoS_2 hybrid nanocomposite for Rhodamine B degradation [24]. A ternary $MoS_2/CdS/Bi_2MoO_6$ Z-scheme heterojunction photocatalyst was synthesized via hydrothermal method by Wang et al. for MB degradation [25]. These studies reported the use of high temperatures and pressures to synthesize these photocatalysts which makes the process tedious and energy intensive. Additionally, these photocatalysts pose challenges in recycling due to the difficulty of separating them from treated wastewater. Therefore, there is a need to develop a composite photocatalyst that can be readily synthesized with improved recoverability for practical usage.

Fe_2O_3 and Fe_3O_4 are visible light active semiconductors with magnetic properties used for photocatalytic degradation of organic pollutants. Fe_2O_3 is a n-type semiconductor with a narrow bandgap, great electrical conductivity, low toxicity and low cost [26,27]. However, Fe_2O_3 suffers from fast electron-hole recombination and weak oxidation ability [27]. This could be overcome by synthesizing a heterojunction interface with MoS_2 to promote charge carrier separation, thus improving the photocatalytic efficacy. Furthermore, loading Graphene Oxide (GO) on this heterojunction interface will provide distinct advantages towards pollutant degradation due to its high conductivity, specific surface area, and efficient electron transfer [28,29].

Herein, we present a simple protocol to prepare a novel, cost-effective, sunlight-responsive, magnetically recoverable photocatalyst based on MoS_2/Fe_2O_3/graphene oxide heterostructure, synthesized via ball-milling and ultrasonication for MB degradation. Compared to the conventional photocatalysts that often require complex synthesis methods with harsh conditions, and face challenges in separation and reusability, this composite offers a scalable, energy-efficient and sustainable alternative for wastewater treatment. The incorporation of Fe_2O_3 and GO enhances the charge carrier separation, extends the absorption of light into the visible spectrum and allows for easy magnetic recovery of the photocatalyst after use, addressing the key limitations in photocatalytic applications. The degradation performance of the photocatalyst was comprehensively evaluated under various operating conditions, including different weight ratios of the catalyst, solution pH, catalyst dosage, initial dye concentration, distance from the light source to the dye solution, light source (UV, solar simulated, visible light and natural sunlight), and the optimum conditions were identified. Additionally, the chemical structure, physical properties, optical properties, morphology, recyclability, and degradation mechanisms were systematically investigated to provide valuable insights for advancing practical large-scale applications of photocatalytic wastewater treatment. The successful development of efficient, reusable, and magnetically recoverable photocatalysts such as MFG composites can not only advance academic understanding but also pave a path for their industrial application in wastewater treatment, dye degradation, and environmental remediation.

2. Experimental section

2.1. Materials

Molybdenum disulfide powder (<2μm, 98 %), Iron (III) oxide (<50 nm, 98 %), methylene blue, isopropyl alcohol, p-benzoquinone (reagent grade, ≥98 %) and ethylenediaminetetraacetic acid (99 %) were purchased from Sigma Aldrich. Hydrochloric acid (32 %) and sodium hydroxide were purchased from Merck. Highly concentrated Graphene oxide slurry (99 % monolayer content) was supplied by Graphenea. All chemicals listed above were used as received without any further purification.

2.2. Synthesis of MoS_2/Fe_2O_3/graphene oxide

Mechanochemical exfoliation approach was used to prepare MoS_2 nanosheets. In a typical process, 0.2 g of bulk MoS_2 along with steel balls with a powder to ball weight ratio of 1:50 were added to a steel milling container within a planetary ball mill (Pulversiette 7, Fritsch). The exfoliation process was carried out at a rotation speed of 400 rpm for 15 hours at room temperature with 10-minute pauses every 30 minutes. After the exfoliation process, the samples were dispersed in DI water. The resulting solution was ultrasonicated for 1 hour and centrifuged at 3000 rpm for 10 minutes to eliminate any unexfoliated MoS_2.

Fe_2O_3 powder and GO were separately dispersed in DI water and sonicated for 10 minutes to get uniform dispersions. Subsequently, the Fe_2O_3 and GO dispersions were added drop by drop onto the MoS_2 dispersion while being subjected to ultrasonication at 45℃. The composite dispersion was ultrasonicated at 45℃ for 1 hour after which it was mixed on a shaker for another hour to obtain a homogeneous dispersion. The resultant dispersion was freeze-dried for 24 h at −86 ℃ and 0.02–0.05 mbar pressure to obtain the nanocomposite powder.

2.3. Characterization

The crystalline structure of the synthesized photocatalysts was

measured with PANalytical X'Pert PRO apparatus with Cu Kα radiation in the 2θ range of 5–70°. Transmission electron microscopy (TEM) images were recorded by JEOL 2100 F microscope operating at 200 kV. Supra 55 VP (ZEISS, Germany) was used to obtain Scanning Electron Microscopy (SEM) images to study the surface morphology of the composite. The Fourier-transform infrared spectroscopy (FT-IR) spectra of the synthesized photocatalysts were measured using the Invenio R spectrometer in the scan range 4000–400 cm^{-1} to identify the functional groups present in the samples. The optical properties of the samples including the optical absorbance, bandgap energy and absorbance of MB in each photocatalytic degradation experiment were recorded on a Cary 300 UV-Vis spectrophotometer in the wavelength range 200–800 nm. The zeta potential of the photocatalysts at various pH values was measured using Zetasizer Nano ZS90. Photoluminescence (PL) intensities of the samples were obtained using Hitachi Fluorescence Spectrophotometer F-4500 at an excitation wavelength of 473 nm to determine the extent of photogenerated electron-hole pair recombination. Thermogravimetric analysis (TGA) curves of the samples were obtained using TA Q50 TGA. The samples were heated from room temperature to 700℃ at a constant heating rate of 20℃/min in a Nitrogen environment. The Quantachrome® ASiQwinTM was used to analyze the surface area of the synthesized samples through Nitrogen adsorption and desorption based on a Brunauer-Emmett-Teller (BET) model.

2.4. Photocatalytic experiments

MB was selected as the target pollutant to investigate the photocatalytic degradation performance of the as-synthesized material. 10 mg of the as-synthesized photocatalyst was added to 100 mL of 10 mg/L methylene blue solution. The dispersion was then subjected to sonication for 5 minutes to eliminate any aggregates and ensure even distribution of the photocatalyst throughout the dye solution. The dispersions were magnetically stirred for 30 minutes in the dark to establish adsorption-desorption equilibrium between the photocatalyst and the dye molecules. Next, the dispersion was irradiated with the light source under constant stirring. To measure the progress of the reaction, aliquots of 2 mL were removed at given time intervals, ranging from 0 to 180 minutes, and subjected to an external magnet to remove the suspended solid photocatalyst. Next, the UV-Vis absorption spectra were measured at a wavelength of 663 nm using the Cary 300 UV-Vis spectrophotometer. The degradation efficiency was calculated using the following equation:

$$\text{Degradation efficiency}(\%) = \frac{(C_o - C_t)}{C_o} \times 100 \quad (1)$$

Where C_o and C_t are the initial and final concentrations of methylene blue at time t_0 and t, respectively.

Langmuir-Hinshelwood's first-order kinetic model shown in Eq. 2 was used to evaluate the photodegradation kinetic mechanism of MB dye by the nanocomposite and to determine the degradation rate constant of the reaction.

$$\ln\frac{C_o}{C_t} = K_{app}t \quad (2)$$

Where C_0 (mg/L) is the initial MB concentration, C_t is the MB concentration at time, t and K_{app} is the degradation rate constant (min^{-1}).

2.5. Free radical scavenger test

The reactive oxygen species responsible for the degradation were explored by adding radical scavengers to the photocatalytic system. 1 mM of isopropyl alcohol (IPA), p-benzoquinone (p-BQ) and ethylenediaminetetraacetic acid (EDTA) were used as hydroxyl radical (·OH), superoxide radical ($\cdot O_2^-$) and h^+ scavengers, respectively in three individual experiments under the same reaction conditions.

3. Results and discussion

3.1. Morphology analysis

The elemental distribution and surface morphology of the composite photocatalyst were conducted by SEM and TEM. The bulk MoS_2 from Fig. 1(a) was crushed and reduced into pieces after ball milling. The composite as shown in Fig. 1(b) and (c) showed a relatively uniform distribution of Fe_2O_3 across the MoS_2 and GO matrix with a lack of significant agglomeration. The Fe_2O_3 appears as spheres deposited on ball-milled MoS_2 sheets and translucent GO sheets. This even distribution facilitated the efficient electron transfer between MoS_2, Fe_2O_3 and GO by maximizing the exposure of active sites to the dye molecules which minimized the likelihood of localized charge recombination. The GO sheets appear to be well integrated with MoS_2 and Fe_2O_3 which contributed to the structural stability of the composite. Additionally, the EDX spectrum of MFG composite is illustrated in Fig. 1(g) and confirms the existence of Mo, O, C, S and Fe in the composite. In addition to the peaks of the composite, no other evident peaks were detected which suggests the high purity of the MFG photocatalyst. Similarly, Fig. 2 depicts the elemental mapping of the MFG composite and indicates that the primary constituents of the composite are Mo, S, Fe, C and O. It can be observed that the sheet-like structures corresponded to MoS_2. At the same time, Fe, C and O were uniformly distributed on the MoS_2 nanosheets.

The TEM images of MoS_2, Fe_2O_3 and MFG nanocomposite are shown in Fig. 1(d-f). As seen in Fig. 1(d), the TEM images of ball-milled MoS_2 showed a nanosheet morphology with average lateral dimension of 175 nm along with a reduction in the number of layers indicating good exfoliation of bulk MoS_2. Fe_2O_3 showed a spherical nature with an average diameter of 45 nm (Fig. 1(e)). The TEM images of the composite (Fig. 1(f)) showed that the MoS_2 nanosheets are sparsely interspersed on the surface of the translucent very thin layer GO sheets with Fe_2O_3 attached on the surface of MoS_2 nanosheets, which confirmed the formation of a heterostructure.

3.2. XRD and FTIR

The crystallographic phase information and purity of the synthesized photocatalyst were studied using XRD. Fig. 3(a) shows the XRD patterns of pristine MoS_2, Fe_2O_3, and MFG composite. The diffraction peaks in the XRD pattern of MoS_2 are in perfect agreement with the MoS_2 crystal standard card. In contrast to the bulk MoS_2, the composite sample has a broad peak at 2θ of ~12.6°, which corresponds to the (002) crystal plane. The decrease in intensity of this peak and its shift to lower diffraction angles in comparison to bulk MoS_2 suggests the decrease in lateral size and thickness, expansion of MoS_2 interlayer spacing and the irregular stacking along the c-direction of the few-layer MoS_2 nanosheets. This expansion of interlayer spacing causes the formation of surface defects and lattice distortion that improves the stability of the MoS_2 nanosheet layers and forms more surface-active edge sites for improved photocatalytic activity [30,31]. The lack of additional peaks corresponding to MoS_2 in the composite suggests the successful exfoliation of bulk MoS_2 to MoS_2 nanosheets via ball-milling [19]. The XRD peaks at 30.2°, 35.6°, 43.3°, 53.8°, 57.3°, and 62.9° could be perfectly indexed to the (104), (110), (113), (116), (018), and (214) crystal planes of Fe_2O_3, respectively (JCPDS Card No. 37–1492). The peak at 30.2° that corresponds to the (104) crystal plane of α-Fe_2O_3 in the composite suggests the successful hybridization of the α-Fe_2O_3 and MoS_2 [32]. Additionally, the co-existence of peaks corresponding to MoS_2 and Fe_2O_3 indicated the formation of MoS_2/Fe_2O_3 heterostructure [33]. The absence of any additional peaks suggests that the sample has high purity. GO is known to have a characteristic peak at 2θ of 12.7° which corresponds to the (001) graphitic plane [34]. This peak was missing in the composite sample possibly due to the superimposition of the (002) plane of MoS_2 on the (001) plane of GO which generated the broad peak at 12.6°.

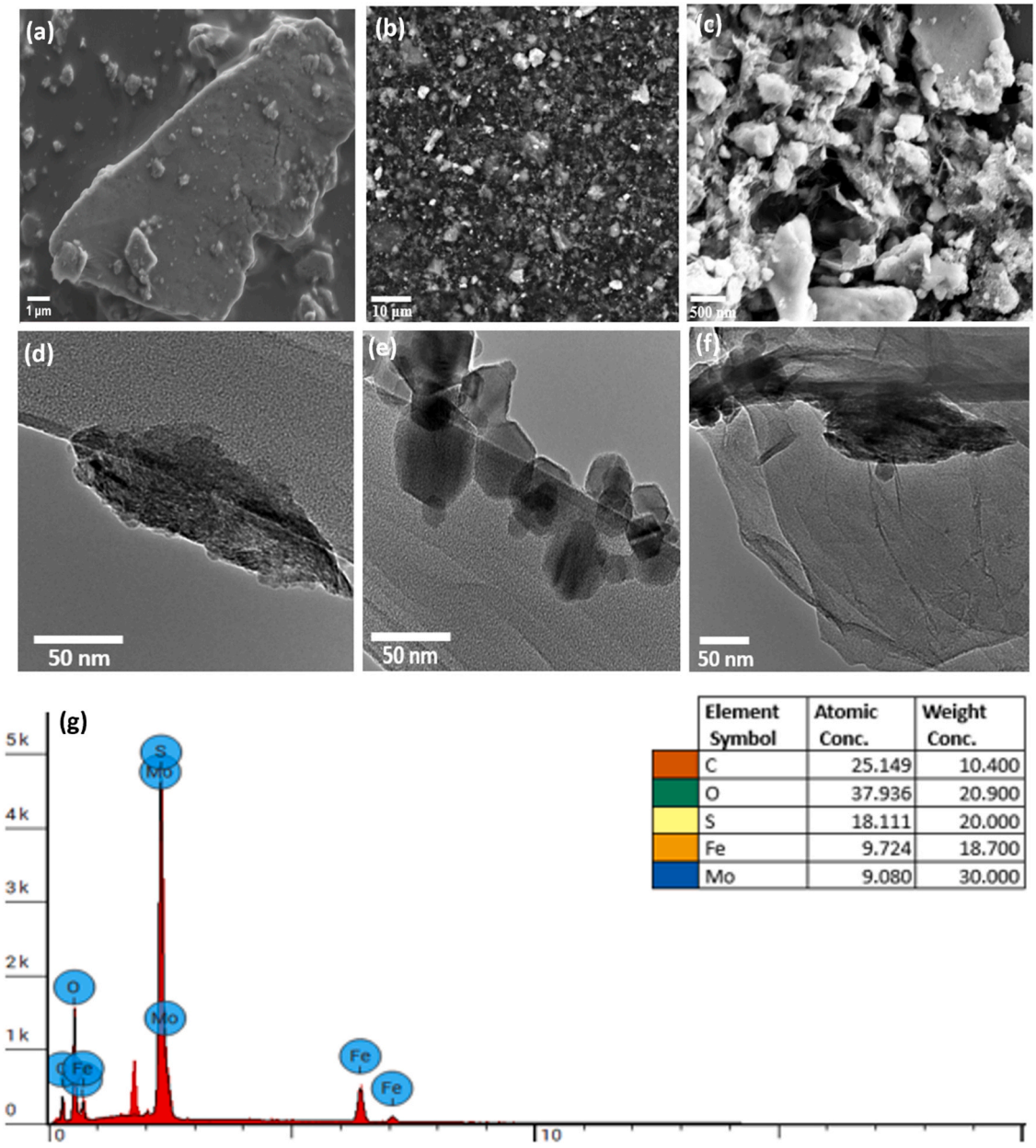

Fig. 1. SEM images of (a) bulk MoS_2, (b-c) MFG nanocomposite, TEM images of (d) ball-milled MoS_2, (e) Fe_2O_3, (f) MFG nanocomposite and (g) EDS and atomic ratios for MoS_2/Fe_2O_3/GO composite.

Additionally, the decrease in peak intensities confirm the formation of the composite material.

FTIR was performed to verify the presence of GO in the composite and to determine its chemical structure (surface functional groups). Fig. 3(b) shows the FTIR spectra of pristine MoS_2, Fe_2O_3, GO and the composite MFG in the spectral range 4000–400 cm^{-1}. The peaks at 560 and 440 cm^{-1} in the FTIR spectra of Fe_2O_3 were attributed to the metal-oxygen stretching vibrational modes. The high-frequency band at 560 cm^{-1} corresponded to the Fe-O deformation in the octahedral and tetrahedral regions. The low-frequency band at 440 cm^{-1} corresponded to the Fe-O deformation in the octahedral region of hematite [35]. The characteristic peaks at 1635 cm^{-1} and the broad band at 3209 cm^{-1} in the GO spectrum corresponded to the C═O group and v(OH) mode of the hydroxyl groups, respectively [36,37]. The FTIR spectra of MoS_2 showed a distinctive minor peak ~460 cm^{-1} which corresponded to the Mo-S vibrational stretching [3]. The bands observed from 1980 to 2150 cm^{-1} are also associated with the MoS_2 structure [38]. The MFG composite showed a combination of peaks from pristine MoS_2, Fe_2O_3, and GO. Additionally, the shift in peak positions and decrease in peak intensity observed in the composite in comparison to the pristine forms signified the decreasing of inter and intramolecular hydrogen bonds formed in the interactions between Fe_2O_3, MoS_2, and GO during the formation of the nanocomposite. The presence of hydroxyl, carboxyl, and metal-oxide groups in the composite improved its adsorption capacity since the anionic functional groups interacted with the cationic dye molecules through electrostatic interactions and Hydrogen bonding, promoting the efficient adsorption of contaminants.

3.3. Optical properties

The UV-Vis absorption spectrum was used to explore the optical absorption properties and band gap of the synthesized photocatalyst as shown in Fig. 3(c). Fe_2O_3 shows absorbance in the range 200–600 nm [39]. GO exhibited an absorption peak at 230 nm which corresponded to

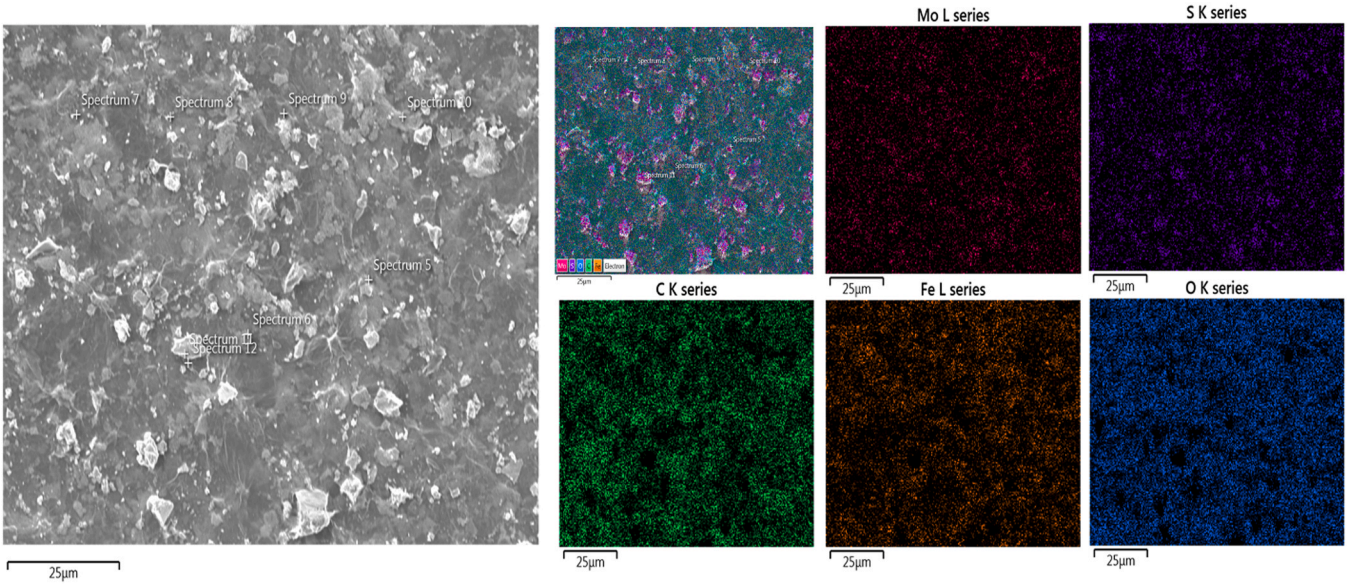

Fig. 2. Elemental mapping of MFG composite.

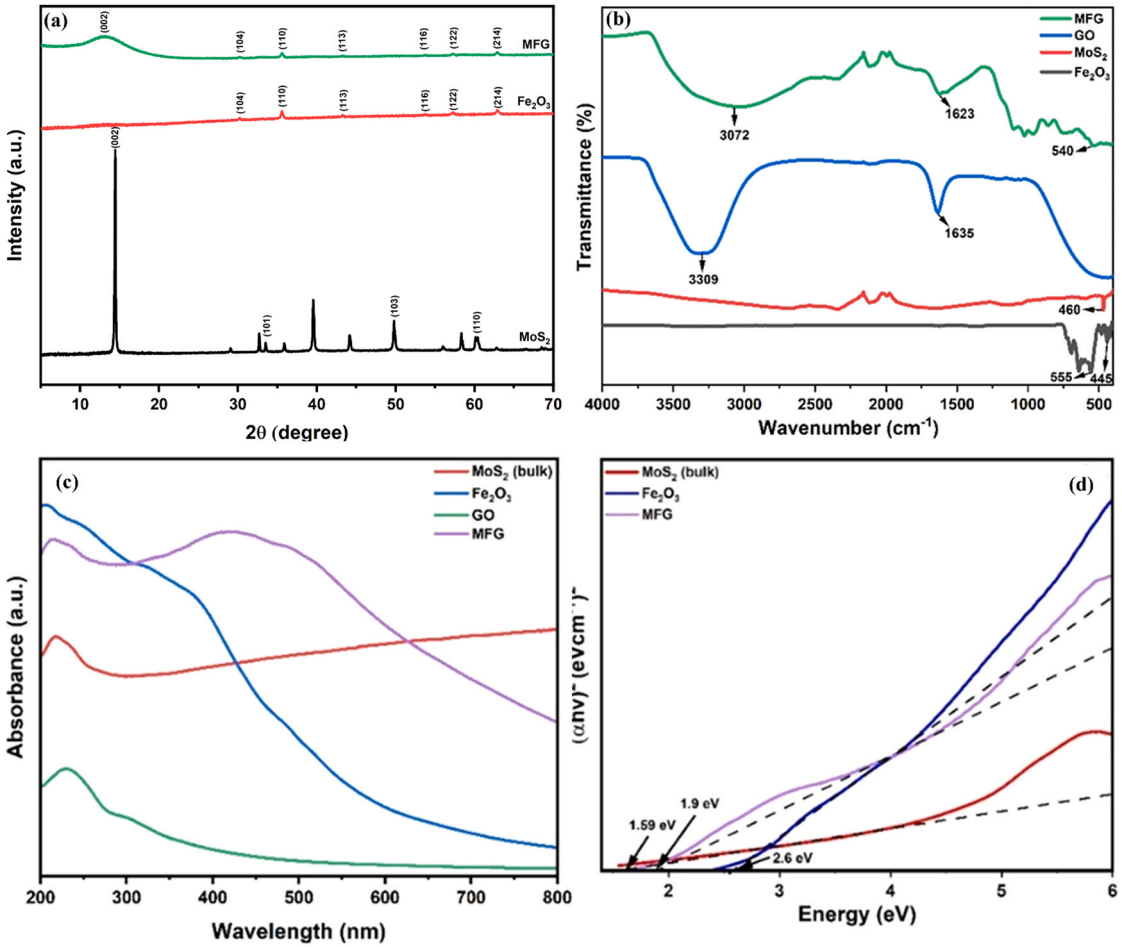

Fig. 3. (a) XRD patterns of MoS_2 (bulk), Fe_2O_3 and MFG, (b) FTIR spectrum of MoS_2(bulk), Fe_2O_3, Graphene Oxide and MFG nanocomposite, (c) UV-Vis absorption spectrum of MoS_2 (bulk), Fe_2O_3, Graphene Oxide and MFG nanocomposite (d) Tauc plot diagram of MoS_2 (bulk), Fe_2O_3 and MFG nanocomposite.

the π-π* transition of the C-C bonds [40]. Hybridization of MoS_2, Fe_2O_3, and GO resulted in a prominent red shift of the absorption edge to higher wavelengths which increased the absorption in the visible light region. These shifts to lower energies could be due to the change in size and layer thickness and the quantum confinement effects of MoS_2 after ball milling upon conversion to nanosheets which agrees with the XRD

findings [38]. The band gaps of the as-synthesized samples were estimated using the Tauc formula:

$$(\propto hv)^n = B(hv - E_g) \quad (3)$$

where E_g is the optical energy band gap, α is the optical absorption coefficient, h is the Planck constant, B is a constant, v is the frequency of the radiation and n is the exponent which can take values 2, and ½ depending on the nature of electronic transition; where n = 2 for indirect band gap materials and n = 1/2 for direct band gap materials [41,42]. Fig. 3(d) shows the Tauc plots for the pristine and composite samples. Based on the Tauc plot, the band gap of pristine MoS_2, Fe_2O_3, and the composite is 1.59 eV, 2.6 eV and 1.9 eV, respectively. The composite has a band gap that falls in between the band gap values of pristine Fe_2O_3 and MoS_2. The band gap is inversely proportional to the particle size [43]. As was disclosed from the XRD results, ball milling reduced the particle size of bulk MoS_2. The higher weight ratio of MoS_2 in comparison to Fe_2O_3 in the composite shifted the band gap energy value from 1.59 eV to 1.9 eV, which corresponded to better absorption in the visible-light region of the electromagnetic spectrum.

The room temperature photoluminescence (PL) spectra of all the samples excited at 473 nm are shown in Fig. 4(a) [44]. The recombination of photogenerated charge carriers can be characterized using the PL intensity in the fluorescence emission spectrum of a semiconductor photocatalyst [26,45]. The weaker the PL intensity generated, the higher the efficiency of separation of photogenerated electrons hole pairs [46]. Pristine MoS_2 and Fe_2O_3 exhibited higher PL intensities, while the composite showed a drastically reduced PL intensity, signifying fluorescence quenching. These results imply the effective charge transfer at the interface due to the heterojunction development between MoS_2, Fe_2O_3 and GO. GO helped in suppressing the recombination of the photogenerated electron hole pairs by migrating the electrons away from MoS_2 and Fe_2O_3, [45,47]. Since the active charged species govern the photocatalytic performance, the composite is expected to exhibit superior photocatalytic performance compared to the pristine forms [48].

TGA was employed in this study to investigate the thermal stability and decomposition behaviour of the composite photocatalyst. As shown in Fig. 4(b), two distinct weight reductions were observed in pristine MoS_2. The first weight loss (2.37 %) was observed up to 420℃ and corresponded to the removal of physisorbed and chemisorbed water molecules [47,48]. The next weight loss (15.85 %) occurred from 420 to 700 C and corresponded to the oxidation of MoS_2 to MoO_3 [48]. The total weight loss was found to be 18.31 %. Fe_2O_3 showed a negligible weight loss of just ~3 %. There was a significant weight loss observed in the TGA curve of GO at around 190 ℃, due to the removal of oxygenated functional groups such as hydroxyl, epoxy, and carboxylate suggesting its thermal instability at higher temperature [49]. In MFG nanocomposite, the weight loss at temperatures below 100 ℃ was attributed to the loss of water molecules. Beyond 100 C, a 6 % weight loss was caused by the thermal degradation of unstable oxygen-containing functional groups, such as hydroxyl, carbonyl, and carboxylic acid which are being pyrolyzed to CO, CO_2, and H_2O [50,51]. Above 500℃, a mass loss of 3.1 % occurred due to the combustion of the carbon skeleton. The higher thermal stability of the MFG nanocomposite indicates the strong affinity between MoS_2 nanosheets, Fe_2O_3, and GO through the formation of a stable ternary nanocomposite.

The surface area of bulk MoS_2 and MFG composite was investigated

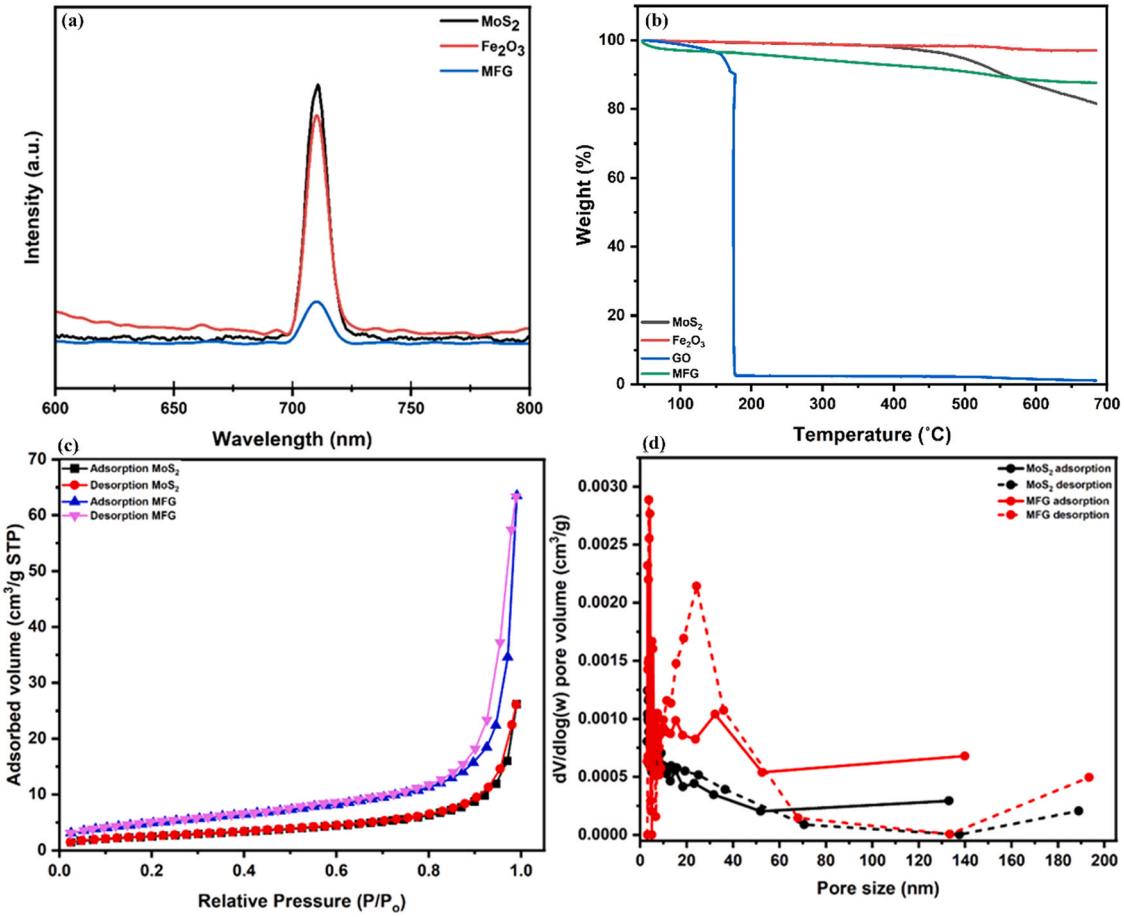

Fig. 4. (a) Photoluminescence (PL) spectrum of MoS_2, Fe_2O_3 and MFG nanocomposite, (b) TGA curve of MoS_2, Fe_2O_3, GO and MFG nanocomposite, (c)N_2 adsorption/desorption isotherm and (b) BJH pore size distribution curve of the photocatalysts.

using Brunauer-Emmett-Teller (BET) technique. According to IUPAC classification, bulk MoS_2 and MFG composite exhibited type IV isotherm curves with H3-type hysteresis loop, revealing a mesoporous structure (2–50 nm) and is represented in Fig. 4(c) [49,50]. The BET surface area of bulk MoS_2 is 9.228 m^2/g while the BET surface area of the MFG composite increased to 18.168 m^2/g. This twofold increase in the surface area of the composite photocatalyst can be attributed to the exfoliation of bulk MoS_2 into thinner two-dimensional layers via ball-milling, which exposes more active sites and reduces particle aggregation. Additionally, the homogeneous dispersion of Fe_2O_3 and GO within the composite prevents restacking of MoS_2 sheets and further enhances the surface area of the composite [51,52]. This increased surface area played a critical role in enhancing the adsorption of MB dye molecules on the surface of the composite photocatalyst which is expected to enhance its photocatalytic activity by increasing the availability of reactive sites for the degradation process [51,53]. Moreover, the higher surface area promotes the interaction with incident light, improving the charge separation and transfer efficiency in the composite.

The Barrett-Joyner-Halenda (BJH) plots confirmed the existence of mesopores in the synthesized composite photocatalyst as shown in Fig. 4 (d). The mesoporosity can be due to the synergistic effect of MoS_2, Fe_2O_3 and GO which creates a more open and accessible pore structure. The higher volume of mesopores enhances the adsorption capacity of the composite by providing more active sites for MB dye molecules to interact with, while facilitating better diffusion of dye molecules into the photocatalyst. This optimized pore structure along with the increased surface area is expected to improve the photocatalytic performance of the composite.

The pH of the solution impacts the number of free radicals generated and the interactions between the photocatalyst and the dye molecules. Zeta potential is a measure of the sign and surface charge of the catalyst in relation to the surrounding conditions. This analysis was used to investigate the surface charge of the photocatalyst at various pH values ranging from pH 1–9 and the results are presented in Figure S2. The point of zero charge of the composite photocatalyst was identified to be 1.3 meaning that the photocatalyst's surface charge is positive below pH 1.3 and negative at pH values greater than 1.3 [54]. The strong electronegativity of the composite was due to the sulfur atoms of MoS_2 and the carbonyl groups and hydroxyl groups at the edges and basal plane of GO, respectively [5,55]. The zeta potential showed a value lower than −30 mV above pH 6. This signified that the colloidal solution was highly stable above pH 6 because of the strong electrostatic repulsion between the particles, preventing its aggregation and settling.

4. Parametric study

4.1. Effect of weight ratio

Different weight ratios of the composite photocatalyst were tested for dye degradation to identify the optimal weight ratio. As shown in Figure S3, MFG (1:1:2) ratio and MFG (1:2:1) showed extremely high adsorption within the first 15 minutes and complete removal within 30 minutes. This was primarily due to the increased presence of hydroxyl and carboxyl groups in the composite, particularly at these ratios, that electrostatically interacted with the cationic methylene blue dye molecules leading to stronger adsorption. However, this extremely high adsorption by the photocatalyst meant that the active sites of the photocatalyst were covered by the adsorbed dye molecules leading to surface saturation inhibiting the penetration of light and reactive species generation, hindering the degradation, and leading to secondary pollution. MFG ratio (2:2:1) showed comparatively lower adsorption within the first 15 minutes but adsorbed over 90 % of the dye molecules in the next 15 minutes. In contrast, the (1:1:1) ratio which shows a moderate adsorption of ~65 % and higher overall degradation (~90 %) demonstrates a more balanced performance, allowing sufficient interaction without fully saturating the surface. However, the (2:1:1) ratio, despite lower adsorption (~35 %) shows enhanced photocatalytic efficiency (~80 %), likely due to more efficient charge separation and reactive species generation. This suggests that while higher adsorption may initially seem beneficial, it can suppress the photocatalytic process by blocking active sites. The (2:1:1) ratio offers a more favourable balance where lower adsorption leaves sufficient active sites for light-driven reactions, causing superior long-term photocatalytic performance compared to both the highly adsorptive and moderately adsorptive ratios. Taking into consideration the photocatalytic degradation efficiency and the abundance of MoS_2 in nature and its low cost in comparison to Fe_2O_3 and GO, MFG (2:1:1) was chosen as the optimum weight ratio for the proceeding experiments.

4.2. Effect of catalyst dosage

Photocatalyst dosage is an important parameter that significantly influences the photocatalytic activity. An economically competitive photocatalyst should achieve maximum degradation efficiency with minimal dosage. The effect of the photocatalyst dose on the degradation of MB was studied by increasing the dose from 0.05 to 0.5 mg/mL at 22℃. According to the results shown in Fig. 5(a), the overall dye removal (adsorption and photocatalysis) increased when the catalyst dosage increased from 0.05 to 0.5 mg/mL. The photocatalytic degradation alone increased when the catalyst dosage increased from 0.05 to 0.25 mg/mL. This could be attributed to the more active sites and generation of charge carriers in the presence of higher catalyst content [7,56]. However, when the catalyst dosage increased beyond 0.25 mg/mL, the prevailing removal mechanism was adsorption. This extremely high adsorption at higher catalyst dosages could be due to the large number of available sites leading to significant adsorption of the dye molecules onto the catalyst surface. Moreover, due to the greater amount of the catalyst in suspension the deeper layers of the catalyst does not get exposed to sufficient light for effective photocatalysis inhibiting the degradation of the adsorbed dye molecules and leading to secondary pollution [57,58]. Since we are interested in the degradation of the dye molecules and not just removal, 0.25 mg/mL was chosen as the optimum photocatalyst dose for the proceeding experiments.

To determine the kinetics of photocatalytic degradation, the collected data were fitted into kinetic equations. The linear relationship observed between ln (C_o/C) and irradiation time, as depicted in Fig. 5 (b), with a high regression coefficient confirms that the photodegradation process follows pseudo-first-order kinetics according to the Langmuir-Hinshelwood model, supporting the hypothesis that the photocatalytic degradation is governed by the availability of active sites and efficient charge transfer. The R^2 values for different catalyst doses of 0.05, 0.1, 0.15, 0.2 and 0.25 mg/mL were 0.86084, 0.91118, 0.96842, 0.97316 and 0.9149 respectively. The highest apparent rate constant was determined to be 0.0098 min^{-1} with 0.25 mg/mL of photocatalyst.

4.3. Effect of pH

The pH of a solution is one of the most important factors that affect the photocatalytic performance of a photocatalyst. To understand the influence of pH on the photocatalytic degradation of MB comprehensively, the pH of the solutions was varied from 4 to 9 with the optimum dose and the results are shown in Fig. 5(c). The pH change of the solution can affect several factors such as the charge and the surface structure of the photocatalyst, the existence of charged radicals in the medium, hydrolysis of the decomposed compound, photolysis rate of oxidant and adsorption trends of reactants [59]. The surface characteristics of heterogeneous catalysts have a substantial impact on the degradation process. As the solution pH changes, the surface charge of the photocatalyst changes. Based on the zeta potential results discussed earlier, the photocatalyst carries a positive charge at pH levels below 1.3 because it undergoes protonation through interactions with the surplus

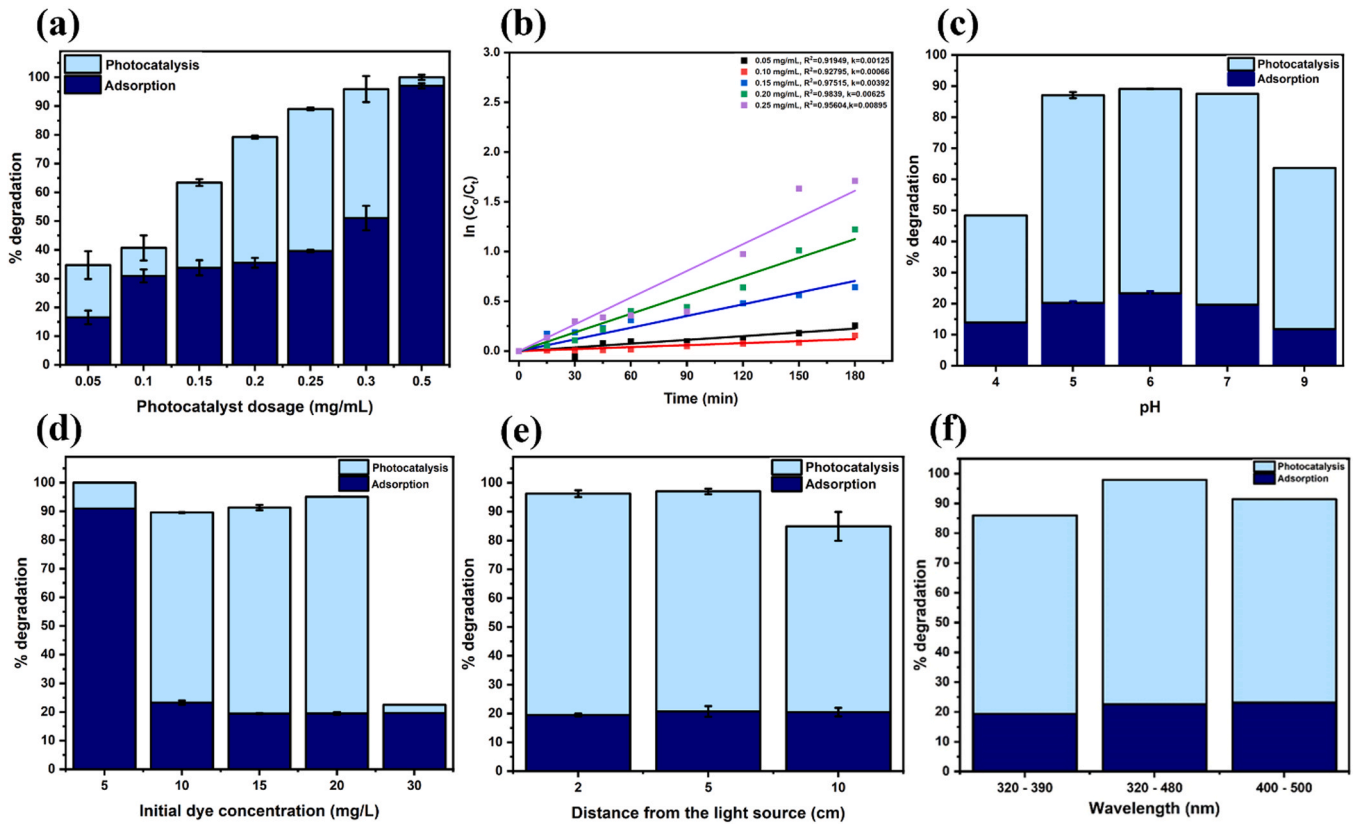

Fig. 5. (a) Effect of photocatalyst dosage on MB degradation (b) Kinetic model of degradation of MB by MFG nanocomposite, (c) Effect of pH, (d) Effect of initial dye concentration and (e) distance between the dye solution and the light source.

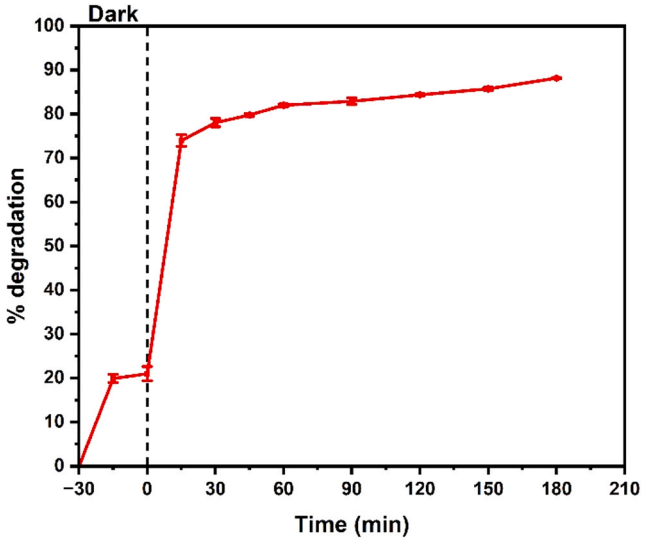

Fig. 6. Photocatalytic degradation of MB under natural sunlight.

hydronium ions in the solution and a negative charge at pH> 1.3 due to deprotonation resulting from reactions with excess hydroxide ions. MB is well recognized as a cationic dye and favours electrostatic attraction between the negatively charged photocatalyst surface and the positively charged dye molecules at pH> 1.3. This improved the adsorption of the cationic dye molecules on the surface of the negatively charged photocatalyst. The photocatalytic performance increased from pH 4–6 as the photocatalyst's surface charge became highly negative and decreased at pH 9. A maximum degradation of 89.9 % was observed at pH 6, with pH 5 and 7 showing closely comparable results. This implied that the photocatalyst was efficient over a wide range of pH and the dye degradation was efficient under weakly acidic and neutral conditions. Although the strongest negative charge on the photocatalyst was recorded at pH 9, this was not evident in the degradation results. This could be due to the aggregation of the photocatalyst that lowered the surface area available for adsorption of the dye molecules at higher pH [60]. Additionally, there can be an increased concentration of hydroxyl groups on the photocatalyst surface at high pH conditions. These hydroxyl groups can act as recombination sites for photogenerated charge carriers and lower the photocatalytic performance. This increased OH^- concentration in the aqueous solution at higher pH also means that relatively less number of H^+ are participating in the photocatalytic reaction, thus inhibiting the photocatalytic degradation.

4.4. *Effect of initial dye concentration*

The influence of the initial dye concentration on photocatalytic degradation performance was investigated by varying the dye concentration from 5 to 30 mg/L at the above-identified optimal conditions. According to the results shown in Fig. 5(d), the highest dye removal was observed at 5 mg/L. There was a slight drop in degradation observed at 10 mg/L initial MB concentration, followed by an increase until 20 mg/L. However, at 30 mg/L dye concentration, a drastic drop in the photocatalytic performance was observed. At 5 mg/L concentration, there are fewer dye molecules present in the solution and more active sites of the photocatalyst for adsorption. Thus, there is a higher adsorption and quicker degradation. Additionally, at lower concentrations, the photon path length was higher leading to a higher absorption of photons by the photocatalyst. On the contrary, although the adsorption may be similar at higher concentrations, the drastic decrease in photocatalytic activity could be due to various factors. The solution is more turbid at higher dye

concentrations, limiting light penetration into the solution. This increases the light scattering and reduces the penetration depth of photons into the solution which lowers the photons reaching the surface of the photocatalyst [61,62]. The excess dye molecules present in the solution will absorb incident light energy themselves, effectively shielding the photocatalyst from receiving adequate photons. This self-shielding effect further reduces the light available for photocatalyst activation, lowering the photocatalytic efficiency. Moreover, the photocatalyst's active sites are saturated with dye molecules, which prevent the generation of reactive oxygen species and reduce the overall photocatalytic activity. Additionally, at higher concentrations, dye molecules tend to aggregate forming dimers and trimers in concentrated solutions which do not interact as efficiently with the active sites of the photocatalyst. The reactive oxygen species produced might not be able to access the aggregated molecules slowing down the degradation process [63,64].

4.5. Effect of distance from the light source

The distance from the light source to the surface of the dye solution is another factor that affects photocatalytic degradation that has not been explored by many researchers [65]. In this study, the distance from the light source to the surface of the dye solution were varied from 2 to 10 cm. The results shown in Fig. 5(e) shows that the photocatalytic degradation observed at a distance of 2 cm and 5 cm were closely comparable. However, increasing the distance from 5 to 10 cm caused a slight reduction in the degradation efficiency due to the lower light intensity reaching the bulk solution [66]. Light intensity decreases with the distance, following the inverse square law. Reduced intensity can lower the excitation of electrons and slow the generation of reactive oxygen species. Moreover, an increase in the distance leads to light scattering which reduces the effective photon flux that reaches the photocatalyst's surface.

4.6. Effect of the light source

The effect of the light source on the degradation efficiency was investigated by using three different filters namely, 320–390 nm (UV light), 320–480 nm (solar light), and 400–500 nm (Visible light) and under natural sunlight as shown in Fig. 5(f) & 6 [67]. As was predicted by the UV-Vis absorbance and Tauc plot results, the nanocomposite photocatalyst showed the highest degradation of 97.9 % under simulated solar light (320–480 nm) showing the pivotal role of MoS_2 in visible light absorbance, followed by visible light alone. The lowest degradation of 86.0 % was observed under UV light (320–390 nm). The higher energy of the photogenerated electron-hole pairs when excited by UV light could also lead to their faster recombination before they can participate in the degradation process. To investigate the practical application of the photocatalytic process, degradation was performed under natural sunlight for 3 hours with all other conditions optimized. The photocatalyst demonstrated an excellent performance, achieving a degradation of 88.2 % under natural sunlight signifying its potential for real-world wastewater treatment and environmental remediation. The performance of the as-synthesized MFG photocatalyst was compared to the photocatalyst synthesized using commercial MoS_2 nanopowder and the results are shown in Figure S6. The commercial photocatalyst showed poor photocatalytic activity which could be due to the lower surface defects, edge sites, and grain boundaries in the commercial MoS_2 nanopowder. Additionally, ball-milling leads to a higher proportion of the metallic 1 T phase in MoS_2 which is more catalytically active compared to the semiconducting 2H phase.

4.7. Free radical scavenger experiments

Heterogeneous photocatalytic reactions are driven by the reactive oxygen species generated. To determine the type of free radicals generated during photocatalysis, free radical scavengers were added to the MB solution. The results are shown in Fig. 7. The addition of all three scavengers (EDTA, p-benzoquinone and IPA) reduced the degradation efficiency confirming the involvement of multiple ROS in the degradation mechanism. The addition of EDTA and p-benzoquinone caused a similar reduction in photocatalytic degradation, while the degradation with IPA was slightly higher. EDTA and p-benzoquinone were utilized to quench the photogenerated holes and superoxide radicals produced while IPA was used to quench hydroxyl radicals [68,69]. These results suggested that holes and superoxide radicals played a major role in degrading MB, while hydroxyl radicals were also involved in the degradation process.

4.8. Recyclability of MoS_2/Fe_2O_3/Graphene oxide

For practical applications, the long-term reusability of the photocatalyst is the most crucial factor. Hence, a series of recyclability tests were performed to assess the reusability of the photocatalyst. The photocatalyst was removed from the dye solution via the use of an external magnet, rinsed with ethanol, and then dried in an oven overnight before being used in the next cycle in fresh MB solution under the same experimental conditions. MFG showed good photocatalytic stability after four consecutive experimental cycles only showing a ~3.5 % reduction in degradation efficiency suggesting that the photocatalyst sites are not significantly blocked by the dye or any of its remaining degradation by-products (Fig. 8(a)). The stability of the photocatalyst was further confirmed by XRD analysis after the degradation cycles and is shown in Fig. 8(b). The XRD results before and after degradation were similar suggesting no phase change or damage to the photocatalyst's crystalline structure. Therefore, this minor loss in photocatalytic activity after the four cycles could be due to the physical loss in photocatalyst during recovery due to its strong attachment to the stir bar owing to its magnetic nature. The results from this study were compared to other ternary photocatalysts from literature to get insights into the photocatalytic performance of the MFG photocatalyst and are presented in Table S1. Compared to other photocatalysts from the literature, the MFG photocatalyst achieved a high degradation with minimal catalyst dosage. This excellent performance can be attributed to the enhanced charge separation and electron transfer efficiency facilitated by the Z-scheme heterostructure.

4.9. Plausible reaction mechanism

The relative energy levels of conduction band minimum (CBM) and valence band maximum (VBM) are key factors in defining the redox power of the photocatalyst [70]. Eqs. (4) and (5) were used to calculate

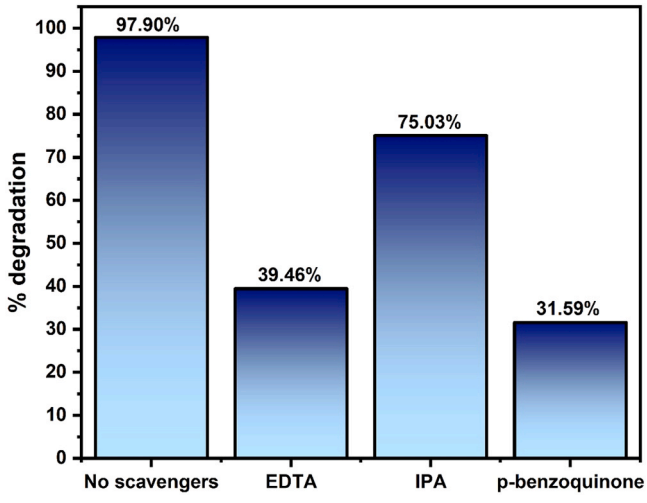

Fig. 7. Effect of scavengers on the photocatalytic degradation of MB.

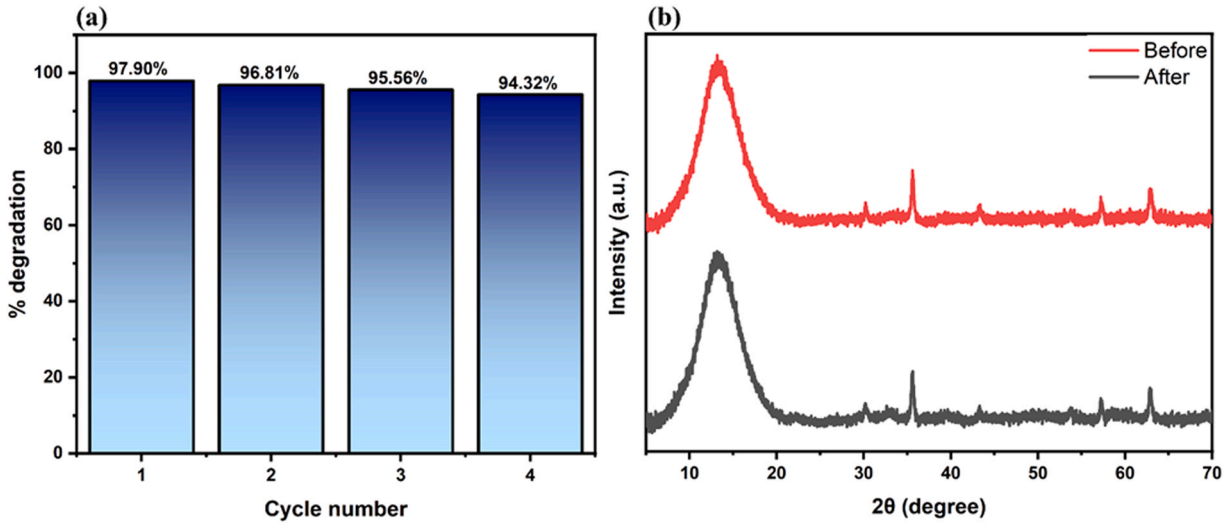

Fig. 8. (a) Recyclability of MFG photocatalyst over 4 successive runs and (b) XRD of MFG before and after four cyclic runs.

the band edge positions of the valence band (E_{VB}) and conduction band (E_{CB}) of MoS_2 and Fe_2O_3 [71].

$$E_{VB} = \chi - E_C + 0.5E_G \quad (4)$$

$$E_{CB} = E_{VB} - E_G \quad (5)$$

Where, E_C is the free energy of the electron on the hydrogen scale, which is about 4.5 eV, χ is the electronegativity of the semiconductor (5.33 for MoS_2 and 4.78 for Fe_2O_3), and E_G is the optical band gap of the semiconductor which was found to be 1.59 eV and 2.6 eV for MoS_2 and Fe_2O_3, respectively from the Tauc plot results. Accordingly, the calculated E_{CB} and E_{VB} of MoS_2 are 0.035 eV and 1.625 eV, respectively while the calculated E_{CB} and E_{VB} of Fe_2O_3 are −1.02 eV and 1.58 eV, respectively. Based on these calculated values for E_{CB} and E_{VB} of Fe_2O_3 and MoS_2, two possible electron transfer mechanisms were speculated for the composite photocatalyst as shown in Fig. 9. It was identified from the quenching experiments that the $\cdot O_2^-$ and h^+ were the major ROS involved in MB degradation.

According to the type-II heterojunction, upon excitation by visible light, the photogenerated electrons will transfer from the CB of Fe_2O_3 to the CB of MoS_2, and the holes will migrate in the opposite direction. Since the position of the CB of MoS_2 is less negative than $E(O_2/\cdot O_2^-)$ (-0.33 eV vs. NHE), the electrons accumulated in the CB of MoS_2 cannot reduce O_2 to $\cdot O_2^-$ [72]. Similarly, the position of the VB of Fe_2O_3 is less positive than the $E(OH^-/\cdot OH)$ (1.99 eV vs. NHE), thus the photoinduced holes accumulated in the VB cannot oxidize OH^- to produce ·OH radicals [73]. The degradation of MB can only occur through the direct oxidation of MB by the holes. This mechanism contradicts the results obtained from the quenching experiments.

On the contrary, according to the Z-scheme heterojunction, the photogenerated electrons will migrate from the CB of MoS_2 to the VB of Fe_2O_3 through GO acting as a solid-state electron mediator where they will recombine. In this mechanism, the accumulated electrons in the CB of Fe_2O_3 and holes in the VB of MoS_2 exhibit stronger redox ability and improved separation efficiency [74]. Since, the photoexcited electrons in the CB of Fe_2O_3 are more negative than the $E(O_2/\cdot O_2^-)$ (-0.33 eV vs. NHE), O_2 will be readily reduced to $\cdot O_2^-$. These $\cdot O_2^-$ generated and the holes in the VB of MoS_2 with the higher oxidizing power will drive the degradation of MB.

Thus, based on the findings of the quenching experiments, it can be deduced that the more plausible charge transfer mechanism in the MFG composite is the direct Z-scheme rather than the type-II mechanism. The direct Z-scheme heterojunction improved photogenerated electron-hole pair separation efficiency and reduced the charge transport path.

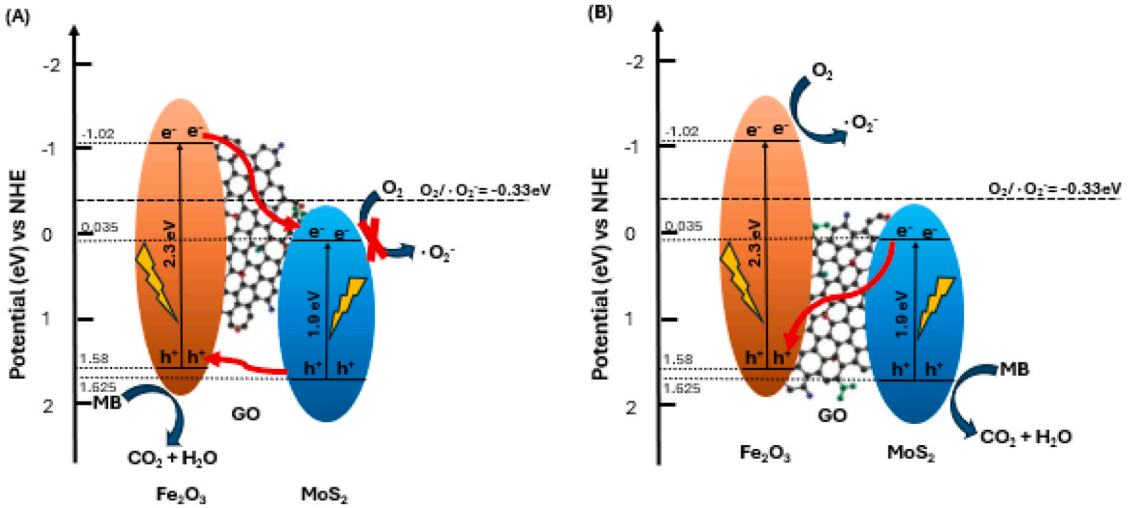

Fig. 9. Possible photocatalytic mechanism for MoS_2/Fe_2O_3/GO (A) Type-II heterojunction (B) Direct Z-scheme heterojunction.

5. Conclusion

MoS_2/Fe_2O_3/graphene oxide Z-scheme photocatalyst was successfully fabricated via ball-milling and ultrasonication and used to degrade MB under solar-simulated and natural sunlight irradiation. The hybrid photocatalyst was thoroughly characterized using various analytical techniques including FTIR, XRD, SEM, TEM, EDX, UV-Visible, BET, and PL spectra. The optimum parameters including solution pH, catalyst dosage, initial dye concentration, distance between the light source and the dye solution, various wavelengths, and reusability experiments were thoroughly examined to attain the maximum degradation efficiency of MB molecules. The results revealed that the MFG photocatalyst showed excellent photocatalytic activity and high MB degradation efficiency of up to 97.90 % within 3 hours of simulated solar light irradiation. Scavenger tests showed that holes and superoxide radicals were the dynamic species accountable for the photodegradation of organic dyes. This increased photocatalytic degradation efficiency of the composite photocatalyst was due to the development of the Z-scheme that improved the separation of charge carriers in addition to improving the oxidation/reduction capability. Notably, photocatalytic experiments under natural sunlight further validated the catalyst's efficiency achieving a degradation of 88.2 % in 3 hours, demonstrating its potential for real-world applications. The photocatalyst also sustained a photocatalytic degradation efficiency of 94.32 % after 4 degradation cycles, demonstrating its potential for reusability. Beyond demonstrating high efficiency, the findings of this study have significant implications for real wastewater treatment applications. The successful performance of the MFG photocatalyst under natural sunlight suggests its feasibility for large-scale implementation in real environmental conditions without using artificial light sources which are energy-intensive. Overall, the findings of this present work provided new insights into the design and synthesis of novel ternary photocatalysts with improved charge separation and stability for the purification and detoxification of dye molecules in wastewater.

CRediT authorship contribution statement

Baskaran Kanagaratnam: Writing – review & editing, Supervision. **Muthukumaran Shobha:** Writing – review & editing, Supervision. **Samarasinghe L. Vishoda:** Writing – review & editing, Writing – original draft, Visualization, Methodology, Conceptualization.

Declaration of Competing Interest

The authors declare that they have no known competing financial interests or personal relationships that could have appeared to influence the work reported in this paper.

Acknowledgements

The authors would like to express their sincere gratitude to Thanojan Jeyachandran from Institute of Frontier Materials, Deakin University for their invaluable assistance in capturing SEM images. We also wish to thank Larruceo Bautista from Victoria University for their expert training on Energy Dispersive X-ray Spectroscopy (EDX) and for generously allowing us to use their facility to obtain SEM images and EDX spectrum. Their support was instrumental in the successful completion of this work. Ms. Samarasinghe gratefully acknowledges Deakin University for the Postgraduate Research Scholarship (DUPR).

Appendix A. Supporting information

Supplementary data associated with this article can be found in the online version at doi:10.1016/j.jece.2025.116813.

Data availability

Data will be made available on request.

References

[1] K. Singha, et al., Chapter 11 - Harmful environmental effects for textile chemical dyeing practice, in: N. Ibrahim, C.M. Hussain (Eds.), Green Chemistry for Sustainable Textiles, Woodhead Publishing, 2021, pp. 153–164.
[2] D. Monga, S. Basu, Enhanced photocatalytic degradation of industrial dye by g-C3N4/TiO2 nanocomposite: role of shape of TiO2, Adv. Powder Technol. 30 (5) (2019) 1089–1098.
[3] D. Monga, S. Basu, Novel MoS2/C3N5 composites with extended spectral response towards highly efficient photocatalytic abatement of hazardous pollutants, J. Environ. Manag. 336 (2023) 117570.
[4] J. Lincho, et al., Nanostructured photocatalysts for the abatement of contaminants by photocatalysis and photocatalytic ozonation: an overview, Sci. Total Environ. 837 (2022) 155776.
[5] H. Zazou, et al., Treatment of textile industry wastewater by electrocoagulation coupled with electrochemical advanced oxidation process, J. Water Process Eng. 28 (2019) 214–221.
[6] E. GilPavas, I. Dobrosz-Gómez, M.Á. Gómez-García, Coagulation-flocculation sequential with Fenton or Photo-Fenton processes as an alternative for the industrial textile wastewater treatment, J. Environ. Manag. 191 (2017) 189–197.
[7] L.V. Samarasinghe, S. Muthukumaran, K. Baskaran, Recent advances in visible light-activated photocatalysts for degradation of dyes: a comprehensive review, Chemosphere 349 (2024) 140818.
[8] Y. Deng, et al., Ultrathin low dimensional heterostructure composites with superior photocatalytic activity: insight into the multichannel charge transfer mechanism, Chem. Eng. J. 393 (2020) 124718.
[9] D. Lan, et al., Adsorptive removal of organic dyes via porous materials for wastewater treatment in recent decades: a review on species, mechanisms and perspectives, Chemosphere 293 (2022) 133464.
[10] X. Zhang, et al., Highly-efficient nitrogen self-doped biochar for versatile dyes' removal prepared from soybean cake via a simple dual-templating approach and associated thermodynamics, J. Clean. Prod. 332 (2022) 130069.
[11] M. Naushad, et al., Adsorption kinetics, isotherm and reusability studies for the removal of cationic dye from aqueous medium using arginine modified activated carbon, J. Mol. Liq. 293 (2019) 111442.
[12] G. Han, et al., Study on the removal of hazardous Congo red from aqueous solutions by chelation flocculation and precipitation flotation process, Chemosphere 289 (2022) 133109.
[13] B. Orero, et al., UV photodegradation of textile dyes using TiO2–ZnO supported on banana peel activated carbon, Int. J. Environ. Sci. Technol. 20 (9) (2023) 9537–9554.
[14] H. Kumari, et al., A review on photocatalysis used for wastewater treatment: dye degradation, Water Air Soil Pollut. 234 (6) (2023) 349.
[15] L.-Z. Huang, et al., Persulfate activation by two-dimensional MoS2 confining single Fe atoms: performance, mechanism and DFT calculations, J. Hazard. Mater. 389 (2020) 122137.
[16] Y. He, Z. Ma, L.B. Junior, Distinctive binary g-C3N4/MoS2 heterojunctions with highly efficient ultrasonic catalytic degradation for levofloxacin and methylene blue, Ceram. Int. 46 (8, Part B) (2020) 12364–12372.
[17] L. Li, et al., Ball-milled MoS2 with graphene shows enhanced catalytic activity for hydrogen evolution reaction, Sci. Technol. Adv. Mater. 25 (1) (2024) 2359360.
[18] N. Luo, et al., S defect-rich ultrathin 2D MoS2: The role of S point-defects and S stripping-defects in the removal of Cr(VI) via synergistic adsorption and photocatalysis, Appl. Catal. B: Environ. 299 (2021) 120664.
[19] Y. Su, et al., Transition metal dichalcogenide (TMD) membranes with ultrasmall nanosheets for ultrafast molecule separation, ACS Appl. Mater. Interfaces 12 (40) (2020) 45453–45459.
[20] A. Meng, et al., Molybdenum sulfide-modified metal-free graphitic carbon nitride/black phosphorus photocatalyst synthesized via high-energy ball-milling for efficient hydrogen evolution and hexavalent chromium reduction, J. Hazard. Mater. 413 (2021) 125400.
[21] C. Ma, et al., Typical layered structure bismuth-based photocatalysts for photocatalytic nitrogen oxides oxidation, Sci. Total Environ. 855 (2023) 158644.
[22] Y. Li, et al., Engineering MoS2 nanomesh with holes and lattice defects for highly active hydrogen evolution reaction, Appl. Catal. B: Environ. 239 (2018) 537–544.
[23] X. Lv, et al., 2D/2D MoS2/ZnIn2S4 heterojunction for simultaneous realization of solar water evaporation and photocatalytic dye degradation, J. Alloy. Compd. 965 (2023) 171382.
[24] M. Nikitha, S.S. Elanchezhiyan, S. Meenakshi, Photodegradation of rhodamine-B in aqueous environment using visible-active gC3N4@CS-MoS2 nanocomposite, Environ. Res. 238 (2023) 117032.
[25] Z. Wang, et al., Construction of MoS2/CdS/Bi2MoO6 Z-scheme photocatalyst for efficient photocatalytic degradation under visible-light, J. Solid State Chem. 322 (2023) 123957.
[26] N. Subha, et al., Heterostructured γ-Fe2O3/FeTiO3 magnetic nanocomposite: an efficient visible-light-driven photocatalyst for the degradation of organic dye, Chemosphere 306 (2022) 135631.
[27] L. Wang, et al., 3D/2D Fe2O3/g-C3N4 Z-scheme heterojunction catalysts for fast, effective and stable photo Fenton degradation of azo dyes, J. Environ. Chem. Eng. 9 (5) (2021) 105907.

[28] T.A. Kurniawan, et al., Functionalizing TiO2 with graphene oxide for enhancing photocatalytic degradation of methylene blue (MB) in contaminated wastewater, J. Environ. Manag. 270 (2020) 110871.
[29] N.A.F. Al-Rawashdeh, O. Allabadi, M.T. Aljarrah, Photocatalytic activity of graphene oxide/zinc oxide nanocomposites with embedded metal nanoparticles for the degradation of organic dyes, ACS Omega 5 (43) (2020) 28046–28055.
[30] Y. Li, et al., Efficient and scalable preparation of MoS2 nanosheet/carbon nanotube composites for hydrogen evolution reaction, Int. J. Hydrog. Energy 45 (33) (2020) 16489–16499.
[31] S. Ji, et al., Exfoliated MoS2 nanosheets as efficient catalysts for electrochemical hydrogen evolution, Electrochim. Acta 109 (2013) 269–275.
[32] L. Chen, et al., A novel nano-heterojunction MoS2/α-Fe2O3 photocatalysts with high photocatalytic and photoelectrochemical performance under visible light irradiation, J. Alloy. Compd. 947 (2023) 169577.
[33] H. Zou, et al., Enhanced degradation of tetracycline via Visible-light-assisted peroxymonosulfate activation over oxygen vacancy rich Fe2O3-CoFe2O4 heterostructures, Sep. Purif. Technol. 314 (2023) 123586.
[34] Z. Ahmad, et al., Decoupling electrochemical parameters of molecular-level-controlled polypyrrole and graphene oxide nanocomposite, Appl. Surf. Sci. 610 (2023) 155464.
[35] R. Jasrotia, et al., Effect of rare earth (Nd3+) metal doping on structural, morphological, optical and magnetic traits of Zn–Mg nano-ferrites, J. Rare Earths 41 (11) (2023) 1763–1770.
[36] U.S. Mondal, et al., Silica sand–supported nano zinc oxide–graphene oxide composite induced rapid photocatalytic decolorization of azo dyes under sunlight and improved antimicrobial activity, Environ. Sci. Pollut. Res. 30 (7) (2023) 17226–17244.
[37] A. Gomathi, et al., Design of ternary CeO2/Fe2O3/reduced graphene oxide-based hybrid nanocomposite for superior photocatalytic degradation material for organic dyes, Dyes Pigments 218 (2023) 111473.
[38] M. Rostami, D.Jahani Sabet, V. Vatanpour, Fabrication of antifouling two-dimensional MoS2 layered PVDF membrane: experimental and density functional theory calculation, Sep. Purif. Technol. 303 (2022) 122226.
[39] K.A. Mohammed, et al., Capping agent effect on optical properties of Fe2O3 nanoparticles, Mater. Today.: Proc. 56 (2022) 2010–2015.
[40] M. Ebrahimi Naghani, et al., Synthesis and characterization of linear/nonlinear optical properties of graphene oxide and reduced graphene oxide-based zinc oxide nanocomposite, Sci. Rep. 13 (1) (2023) 1496.
[41] P. Sharma, M.K. Singh, M.S. Mehata, Sunlight-driven MoS2 nanosheets mediated degradation of dye (crystal violet) for wastewater treatment, J. Mol. Struct. 1249 (2022) 131651.
[42] M.I. Khan, et al., Structural, electrical and optical properties of hetrostructured MoS2/ZnO thin films for potential perovskite solar cells application, J. Mater. Res. Technol. 20 (2022) 1616–1623.
[43] S. Saleem, et al., Analysis and characterization of opto-electronic properties of iron oxide (Fe2O3) with transition metals (Co, Ni) for the use in the photodetector application, J. Mater. Res. Technol. 25 (2023) 6150–6166.
[44] H. Choi, et al., Enhanced optical absorption in conformally grown MoS2 layers on SiO2/Si substrates with SiO2 nanopillars with a height of 50 nm, Nanoscale Adv. 3 (3) (2021) 710–715.
[45] H.M. El Sharkawy, et al., Efficient photocatalytic degradation of organic pollutants over TiO2 nanoparticles modified with nitrogen and MoS2 under visible light irradiation, Sci. Rep. 13 (1) (2023) 8845.
[46] A. Jenifer, S. Sriram, Enhanced photocatalytic organic dye degradation activities of pristine and Zn-doped V2O5 nanoparticles, Appl. Surf. Sci. 611 (2023) 155629.
[47] O.T. Mahlangu, G. Mamba, B.B. Mamba, A facile synthesis approach for GO-ZnO/PES ultrafiltration mixed matrix photocatalytic membranes for dye removal in water: Leveraging the synergy between photocatalysis and membrane filtration, J. Environ. Chem. Eng. 11 (3) (2023) 110065.
[48] J. Swain, et al., Photocatalytic dye degradation by BaTiO3/zeolitic imidazolate framework composite, J. Alloy. Compd. 965 (2023) 171438.
[49] S.S. Patil, et al., Facile one-pot synthesis of ternary Fe doped Cu-ZnO nanocatalyst: an efficient and recyclable solar light driven photocatalyst, Surf. Interfaces 48 (2024) 104255.
[50] V. Jeyalakshmi, et al., Carbon vacancy modified g-C3N4 hollow tubes-iron oxide composite for photocatalytic application, J. Environ. Chem. Eng. 12 (6) (2024) 114113.
[51] P. Zhu, et al., Construction of 3D flower-like FeTiO3/MoS2 heterostructure photocatalyst for degradation of tetracycline hydrochloride, J. Alloy. Compd. 937 (2023) 168425.
[52] X. Li, et al., Enhanced activation of peroxymonosulfate by ball-milled MoS2 for degradation of tetracycline: boosting molybdenum activity by sulfur vacancies, Chem. Eng. J. 429 (2022) 132234.
[53] R.A. El-Gendy, et al., Metal chalcogenides (CuS or MoS2)-modified TiO2 as highly efficient bifunctional photocatalyst nanocomposites for green H2 generation and dye degradation, Sci. Rep. 13 (1) (2023) 7994.
[54] J. Kisała, R. Wojnarowska-Nowak, Y. Bobitski, Layered MoS2: effective and environment-friendly nanomaterial for photocatalytic degradation of methylene blue, Sci. Rep. 13 (1) (2023) 14148.
[55] I. Ferrari, et al., Understanding the nature of graphene oxide functional groups by modulation of the electrochemical reduction: a combined experimental and theoretical approach, Carbon 203 (2023) 29–38.
[56] O. Samuel, et al., WO3–based photocatalysts: a review on synthesis, performance enhancement and photocatalytic memory for environmental applications, Ceram. Int. 48 (5) (2022) 5845–5875.
[57] S. Kalikeri, et al., Visible light-induced photocatalytic degradation of Reactive Blue-19 over highly efficient polyaniline-TiO2 nanocomposite: a comparative study with solar and UV photocatalysis, Environ. Sci. Pollut. Res. 25 (4) (2018) 3731–3744.
[58] P. Jansanthea, et al., Green synthesis of CuO/Fe2O3/ZnO ternary composite photocatalyst using grape extract for enhanced photodegradation of environmental organic pollutant, Chemosphere 351 (2024) 141212.
[59] Y. Vasseghian, et al., A hybrid nanocomposite based on CuFe layered double hydroxide coated graphene oxide for photocatalytic degradation of trimethoprim, Chemosphere 322 (2023) 138243.
[60] T. Nawz, et al., Graphene to advanced MoS2: a review of structure, synthesis, and optoelectronic device application, Crystals 10 (2020), https://doi.org/10.3390/cryst10100902.
[61] N. Tahir, et al., Impact of alternate Mn doping in ternary nanocomposites on their structural, optical and antimicrobial properties: comparative analysis of photocatalytic degradation and antibacterial activity, J. Environ. Manag. 337 (2023) 117706.
[62] A. Nawaz, et al., Fabrication and characterization of new ternary ferrites-chitosan nanocomposite for solar-light driven photocatalytic degradation of a model textile dye, Environ. Technol. Innov. 20 (2020) 101079.
[63] A. Fernández-Pérez, G. Marbán, Visible light spectroscopic analysis of methylene blue in water; what comes after dimer? ACS Omega 5 (46) (2020) 29801–29815.
[64] H.A. Wani, et al., Applications of spectroscopic techniques to the study of monomer–dimer equilibria for methylene blue in aqueous solutions containing ionic liquid: probing the structural interactions involving water and ionic liquids, Spectrochim. Acta Part A: Mol. Biomol. Spectrosc. 287 (2023) 122058.
[65] K.P. Sundar, S. Kanmani, Progression of Photocatalytic reactors and it's comparison: a review, Chem. Eng. Res. Des. 154 (2020) 135–150.
[66] R. Keyikoğlu, et al., Synthesis of visible light responsive ZnCoFe layered double hydroxide towards enhanced photocatalytic activity in water treatment, Chemosphere 309 (2022) 136534.
[67] M. Laghaei, et al., Facile electrochemical anodisation for generating nanopores across visible light-responsive cerium-titanium oxide heterojunctions for environmental remediation, J. Environ. Chem. Eng. 11 (5) (2023) 110341.
[68] B. Parasuraman, et al., Designing the heterostructured FeWO4/FeS2 nanocomposites for an enhanced photocatalytic organic dye degradation, Chemosphere 334 (2023) 138979.
[69] J. Zheng, et al., Barium titanate/ZnAl-layered double hydroxide catalysts for piezoelectrically enhanced photocatalytic degradation of coexisting pollutants and antibiotic resistance genes, J. Environ. Chem. Eng. 12 (6) (2024) 114227.
[70] Y.R. Girish, et al., Rapid and facile synthesis of Z-scheme ZnO/g-C3N4 heterostructure as efficient visible light-driven photocatalysts for dye degradation and hydrogen evolution reaction, J. Hazard. Mater. Adv. 9 (2023) 100230.
[71] Y. Naciri, et al., Influence of Sr-doping on structural, optical and photocatalytic properties of synthesized Ca3(PO4)2, J. Colloid Interface Sci. 572 (2020) 269–280.
[72] L. Wang, et al., Developing a Z-scheme Ag2CO3/ZIF-8 heterojunction for the surface decoration of cotton fabric toward repeatable photocatalytic dye degradation, Appl. Surf. Sci. 610 (2023) 155605.
[73] T. Qiang, et al., Dual modified MoS2/SnS2 photocatalyst with Z-scheme heterojunction and vacancies defects to achieve a superior performance in Cr (VI) reduction and dyes degradation, J. Clean. Prod. 291 (2021) 125213.
[74] R.R. Nallapureddy, et al., Z-scheme photocatalysis and photoelectrochemical platform with a Co3O4-CuO heterogeneous catalyst for the removal of water pollutants and generation of energy, J. Clean. Prod. 382 (2023) 135302.